Aerodynamic Performance of an Aircraft with Aft-Fuselage Boundary Layer Ingestion Propulsion

della Corte, B.; van Sluis, M.; Gangoli Rao, A.; Veldhuis, L.L.M.

DOI
10.2514/6.2021-2467

Publication date
2021

Document Version
Final published version

Published in
AIAA AVIATION 2021 FORUM

AIAA AVIATION Forum
August 2-6, 2021, VIRTUAL EVENT
AIAA AVIATION 2021 FORUM

10.2514/6.2021-2467

Aerodynamic Performance of an Aircraft with Aft-Fuselage Boundary Layer Ingestion Propulsion

Biagio Della Corte *, Martijn van Sluis †, Arvind Gangoli Rao‡, and Leo L. M. Veldhuis§
Faculty of Aerospace Engineering, Delft University of Technology, Delft, The Netherlands

Boundary Layer Ingestion (BLI) is a technology that promises fuel consumption benefits for future civil aircraft. However, it introduces detrimental aerodynamic interactions between the propulsor and the airframe. In particular, the inflow to the BLI propulsor is affected by the flow around the airframe elements. The non-uniform inflow can influence the fan aerodynamic, aeroacoustic and aeroelastic performance. As a consequence, the fan design needs to tolerate the inlet distortions in all the flight phases. This paper discusses an experimental study of the aerodynamic performance of an aircraft with a BLI propulsor integrated at the aft-fuselage section, representative of a Propulsive Fuselage Concept (PFC) aircraft. Aerodynamic load measurements show that the BLI propulsor affects the longitudinal and lateral-directional equilibrium of the aircraft in off-cruise conditions. Flow measurements at the BLI propulsor inlet indicate that the fuselage boundary layer induces the strongest total pressure distortion. However, particularly at a non-zero sideslip angle, the vertical tail plane strongly affects the inflow to the BLI propulsor, introducing non-symmetric total pressure and velocity distortions. The analysis of the momentum and power fluxes in the flowfield show that around 20% of the total aircraft drag is produced in the fuselage boundary layer, while around 5% of the total aircraft drag power is dissipated in the fuselage wake. Furthermore, the BLI propulsor substantially reduces the axial kinetic energy flux in the fuselage boundary layer (the so-called "wake-filling" effect), suggesting an increased propulsive efficiency.

Nomenclature

Acronyms

BF	Bare Fuselage
BL	Boundary Layer
BLI	Boundary Layer Ingestion
LTT	Low Turbulence Tunnel
PF	Powered Fuselage
PFC	Propulsive Fuselage Concept
PIV	Particle Image Velocimetry
VTP	Vertical Tail Plane

Abbreviations

CDI	Circumferential distortion index
DC(60)	Distortion index based on a 60° sector
RDI	Radial distortion index

Non-dimensional Coefficients

$C_{\mathcal{L}}$	Roll moment coefficient, $\mathcal{L}/q_\infty Sc$
$C_{\mathcal{M}}$	Pitch moment coefficient, $\mathcal{M}/q_\infty Sc$
$C_{\mathcal{N}}$	Yaw moment coefficient, $\mathcal{N}/q_\infty Sc$
C_D	Drag coefficient, $D/q_\infty S$
C_L	Lift coefficient, $L/q_\infty S$
C_{p_t}	Total pressure coefficient, $(p_t - p_{t\infty})/q_\infty$
C_Y	Lateral force coefficient, $Y/q_\infty S$

Greek Symbols

α	Angle of attack, [°]
β	Angle of sideslip, [°]

*Ph.D. Candidate, Flight Performance and Propulsion Group; email: B.DellaCorte@tudelft.nl
†Ph.D. Candidate, Flight Performance and Propulsion Group
‡Associate Professor, Flight Performance and Propulsion Group; email: A.GangoliRao@tudeflt.nl
§Full Professor, Section Head, Flight Performance and Propulsion Group

Γ Circulation, [m^2/s]

μ Dynamic viscosity, [Pa s]

Ω Fan angular velocity, [rad/s]

ω Vorticity, [s^{-1}]

ϕ Azimuthal angular position, [°]

ψ Radial angle, [°]

ρ Density, [kg/m^3]

θ Swirl angle, [°]

Latin Symbols

$\dot{E}_a$ Axial kinetic energy flow rate, [W]

$\dot{E}_p$ Pressure work rate, [W]

$\dot{E}_v$ Transverse kinetic energy flow rate, [W]

$\mathcal{L}$ Roll moment, [N m]

$\mathcal{M}$ Pitch moment, [N m]

$\mathcal{N}$ Yaw moment, [N m]

c Wing mean aerodynamic chord, [m]

c_f Fan mid-span chord, [m]

D Drag force, [N]

$d\dot{E}_a$ Axial kinetic energy flux density, [W/m^2]

$d\dot{E}_p$ Pressure work density, [W/m^2]

$d\dot{E}_v$ Transverse kinetic energy flux density, [W/m^2]

D_0 Reference drag force, [N]

D_f Fan diameter, [m]

dF_a Axial momentum flux density, $dF_a = -dF_x$ [N/m^2]

dF_x Axial momentum flux density, [N/m^2]

F_a Axial momentum flow rate, $F_a = -F_x$ [N]

F_i i-th component of the BLI propulsor inflow

F_x Axial momentum flow rate, [N]

L Lift force, [N]

L_b Fuselage body length, [m]

p Pressure, [Pa]

p_t Total pressure, [Pa]

q Dynamic pressure, [Pa]

R_b Fuselage body radius, [m]

Re_c Mean-chord-based Reynolds number, $Re_c = \rho_\infty V_\infty c/\mu_\infty$

S Wing planform area, [m^2]

u, v, w Cartesian velocity components, [m/s]

u, v_r, v_t Cylindrical velocity components, [m/s]

U_tip Fan tip speed, [m/s]

V Velocity magnitude, [m/s]

x, r, ϕ Body reference system

x, y, z Cartesian coordinates

x_B, y_B, z_B Body reference system

Y Side force, [N]

Sub-scripts

∞ Freestream conditions

I. Introduction

Boundary Layer Ingestion (BLI) is an airframe-propulsion integration technology that enables unconventional aircraft architectures to benefit from increased aero-propulsive efficiencies. Historically, the potential advantage of operating a propeller in a viscous wake has long been known in the field of marine propulsion [1, 2]. A milestone study pioneered BLI for aircraft propulsion and related the propeller and wake properties to quantify the power saving [3]. More recently, the physical mechanisms of this benefit were explained through power-based flow analysis methods. First, the kinetic energy transported and dissipated in the wake of the aircraft is reduced (the so-called "wake-filling" effect of BLI). Second, the kinetic energy in the boundary layer and ingested by the propulsor results in a reduction of the required mechanical power (see Ref. [4–6]).

In the last decade, BLI has been investigated in numerous unconventional aircraft concepts with an estimated power benefit over a conventional airchitecture ranging from 5% to 10% [7, 8]. One of the most promising configuration is the Propulsive Fuselage Concept (PFC), a tube-and-wing aircraft where an aft-fuselage mounted BLI propulsor ingests the

fuselage boundary layer [9–11]. The PFC has various advantages over other BLI configurations. First, momentum deficit share which can be ingested with a single propulsor is maximized [12]. Moreover, the inlet distortions for the BLI propulsor are minimized, since the fuselage boundary layer can ideally be axisymmetric, resulting in minimum propulsor losses [13]. Finally, the airframe design changes are minimzed since the PFC implements BLI on an otherwise conventional architecture [11].

The CENTRELINE project, funded by EU within the Horizon 2020 framework, proposed a turbo-electric PFC for a long-range wide-body commercial aviation aircraft [11]. The concept, sketched in Fig. 1, featured an aft-fuselage mounted shrouded fan driven by an electric motor powered by the under-the-wing turbofans. During cruise, the BLI propulsor provides around 25% of the total propulsive power to maximize the system-level benefit [14]. Both the fuselage and the fan stage were designed assuming axisymmetric conditions. Numerical work optimized the axisymmetric fuselage and shroud contours to maximize the propulsive force for a given shaft power [15]. At the same time, the fan stage design minimized the losses in efficiency induced by the inlet distortions due to the fuselage boundary layer [13]. A previous related work has experimentally investigated the aerodynamic performance of an axisymmetric propulsive fuselage representative of the CENTRELINE concept [16]. The study analyzed the aerodynamic interactions between the fuselage airframe and the BLI propulsor in axial inflow conditions. The work highlighted that the propulsor has a strong effect on the fuselage boundary layer. Due to the suction imposed to the fluid, higher velocity is found in the near-wall region of the boundary layer upstream of the propulsor and high momentum flow is drawn toward the fuselage wall, which reduces the local boundary layer thickness.

However, in a more realistic scenario, the flow around the fuselage aft-section is not expected to be axisymmetric, as it will result from the influences of different elements. In particular, the fuselage-mounted shrouded fan will be affected by other aerodynamic surfaces and elements of the aircraft, namely the wing and vertical tail plane. These elements will introduce total pressure and velocity distortions at the fan inlet due to viscous dissipation (i.e. boundary layers and wakes) or circulation (i.e. lift) which are a function of the flight conditions. These distortions can have an impact on propulsive efficiency, stall margin, aeromechanic and aeroacoustic performance of the fan [17–21]. Moreover, the aerodynamic interaction between the BLI propulsor and the aircraft airframe can have an effect on the overall system aerodynamic performance and influence the local flowfield around the fuselage aft-cone section. A schematic of the main flow distortions and aerodynamic interaction expected in the propulsive fuselage is presented in Fig. 1.

In order to tailor the PFC design to minimize installation penalties and hence maximize the aero-propulsive efficiency, the main flow phenomena need to be investigated. This paper discusses an experimental analysis of an aircraft model representative of the CENTRELINE Propulsive Fuselage Concept. The model featured a shrouded BLI propulsor integrated at the aft fuselage section. The goal of the low-speed wind-tunnel experiments was twofold. First, to assess the effect of the BLI fan on the aircraft forces in various flight conditions. Second, to characterize the aerodynamic flow around the BLI propulsor in on- and off-design conditions.

II. Methods

Low-speed wind-tunnel tests were performed on a sub-scaled aircraft model equipped with a fuselage-mounted BLI shrouded fan. As a consequence of the scaling limitations, the Reynolds and Mach numbers characterizing the flow at the

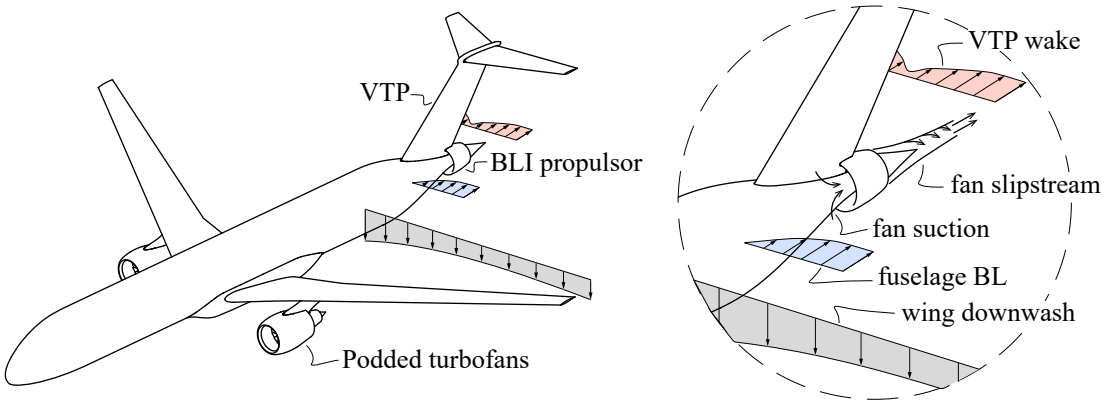

Fig. 1 Schematic of the CENTRELINE Propulsive Fuselage Concept. Based on [11, 13].

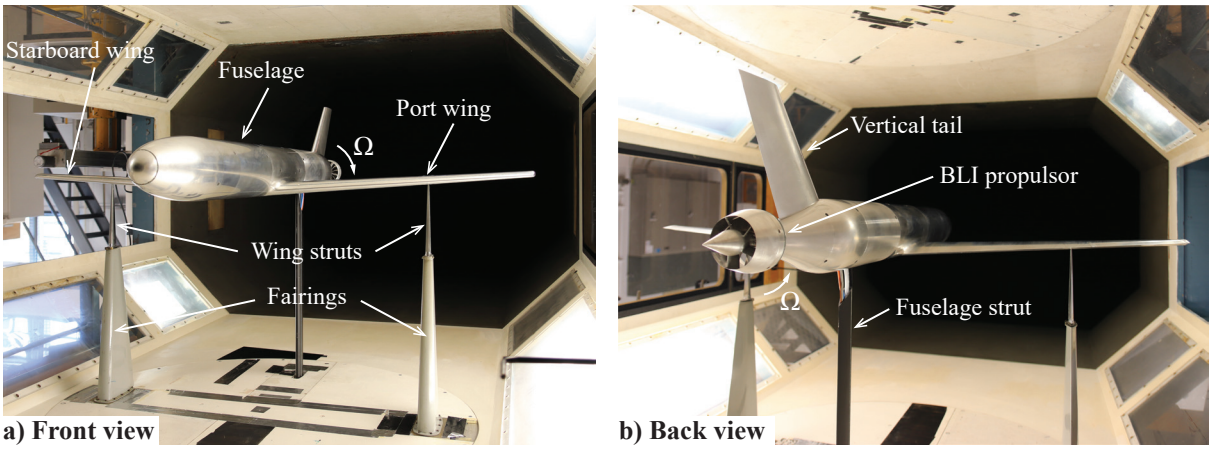

Fig. 2 Photographs of the wind-tunnel setup assembled in the test section of the Low Turbulence Tunnel of Delft University of Technology.

lab scale were lower than the expected values in typical high-subsonic cruise conditions. In particular, due to the lower Reynolds number obtained during the experiments, delayed turbulent transition and relatively larger boundary layer thicknesses were expected compared to the full-scale flight conditions. To mitigate these effects, the transition locations were imposed on all the fixed aerodynamic surfaces through tripping elements. Moreover, the BLI propulsor model was sized accordingly to the fuselage boundary layer thickness to maintain the same scaling relative to the boundary layer thickness as found in full-scale aircraft. Compressibility effects could not be simulated in the low-speed wind-tunnel used. Compressibility effects play a major role in the aerodynamics of lifting surfaces (i.e. wings). However, the consequences of the low Mach number are not expected to have a strong influence on the flow around the fuselage body, since the critical Mach number of axisymmetric bodies is lower than the typical cruise Mach number (see for example Ref. [22–24]).

Furthermore, the aircraft model tested was representative of the CENTRELINE Propulsive Fuselage Concept design. However, except for some aspects (e.g. the contour of the fuselage aft-cone), the model design was simplified to avoid that configuration-specific design choices could affect some of the findings of this study.

In general, the aerodynamic scaling and the model design could have an effect on the quantitative results of the experimental investigations carried out during this study. However, the fundamental interaction mechanisms between the BLI propulsor and the airframe were effectively simulated in the wind-tunnel experiments in a qualitative sense. As a consequence, the same mechanisms are expected to occur in the full-scale flight conditions, even though possibly with different magnitudes.

A. Wind-Tunnel Facility and Setup

The wind-tunnel experiments were carried out at the Low Turbulence Tunnel (LTT) of Delft University of Technology. The LTT is a closed-loop, closed test-section atmospheric wind-tunnel. The test section features and octagonal cross-section with a width of 1.80 m and height of 1.25 m. The maximum test speed that can be reached is 120 m/s with a turbulence intensity below 0.1%.

The test setup consisted of an aircraft model representative of the CENTRELINE Propulsive Fuselage Concept (PFC). Photographs of the model installed in the test section are shown in Fig. 2 and the main model dimensions are reported in Fig. 3. The reference systems and conventions used in the current study are reported in Fig. 4.

The aircraft model was mounted to an external six-components balance through a three-point attachment system. The support structures were hinged to the two wings and to the aft-fuselage section. The model could rotate around the wing-support hinge axis to simulate an angle of attack, α, which was controlled by vertically sliding the aft-fuselage support. In addition, the model could rotate around the vertical axis to simulate an angle of sideslip, β. The support struts rotated with the model and with a turntable embedded in the test-section wall.

The fuselage consisted of an axisymmetric body with a maximum radius, R_b, of 70 mm and a total length, L_b, of 1564 mm. The fuselage aft-cone section shape was adapted from the propulsive aft-cone of the CENTRELINE PFC aircraft. Moreover, the fuselage aft-cone section was modular, allowing the testing of different configurations which are

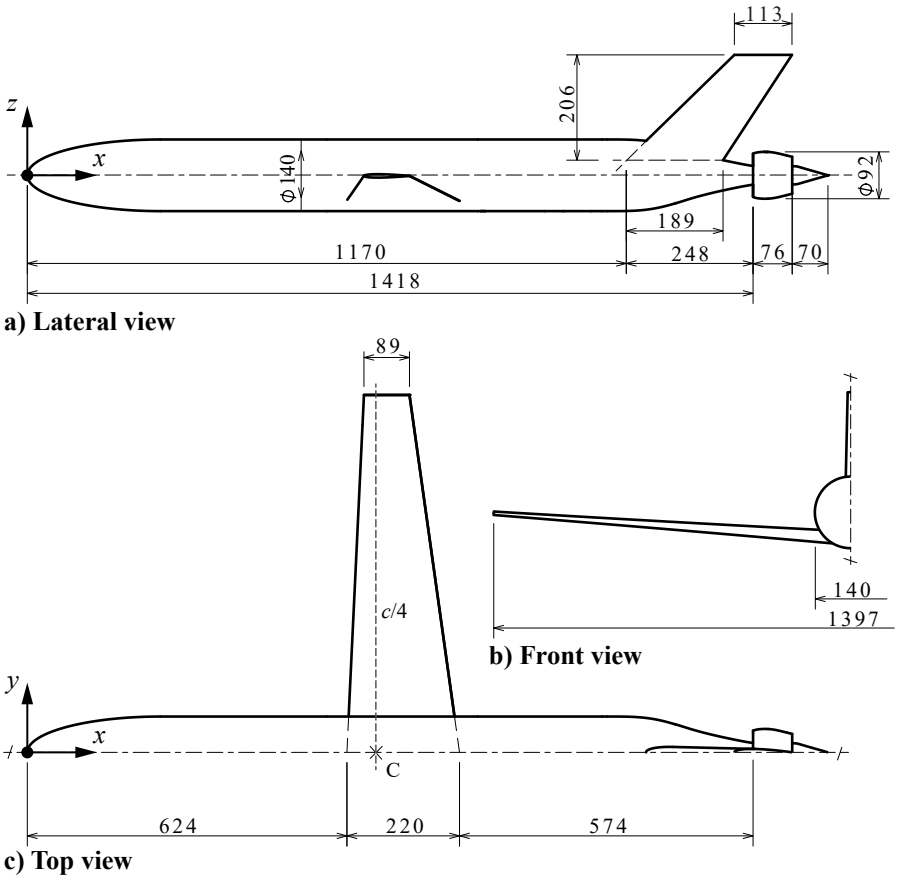

Fig. 3 Technical views of the wind-tunnel model (dimensions in mm).

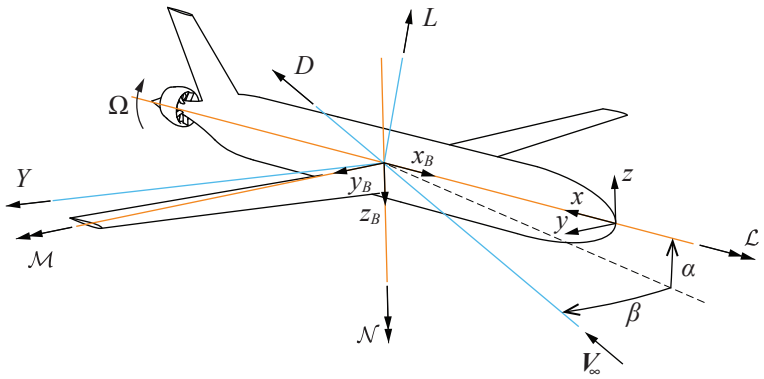

a) Aircraft attitude angles, forces and moments conventions

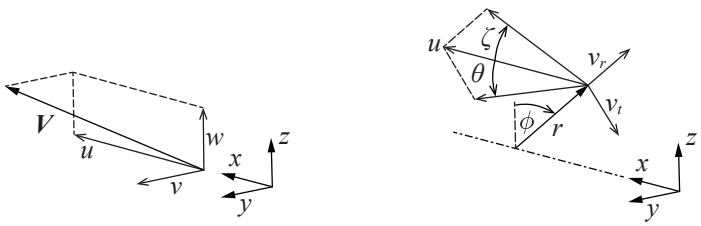

b) Cartesian velocity components **c) Cylindrical velocity components**

Fig. 4 Conventions and definitions used for the aircraft forces and moments and velocity components.

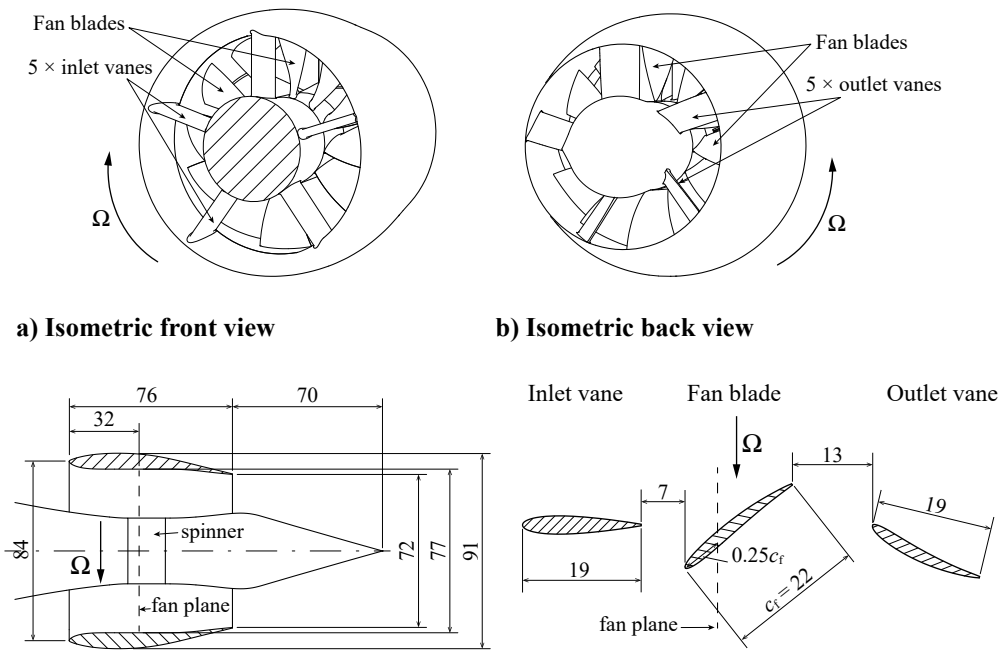

Fig. 5 Details of the shrouded BLI propulsor equipping the wind-tunnel model (dimensions in mm).

described in more detail in Sec. II.C.1.

The fuselage aft-cone section was equipped with a BLI shrouded propulsor, of which technical views and details are shown in Fig. 5. The fan featured 12 blades with a diameter, D_f, of 75 mm, an hub-to-tip-radii ratio of 0.41 and a mid-span blade chord, c_f, of 22 mm. The fan was driven by a three-phase brushless electric motor and its rotational speed, Ω, was measured through an US Digital© optical encoder mounted on the motor shaft.

Since the fuselage boundary layer is expected to be relatively larger at the test scale when compared to the flight scale (due to the lower Reynolds number), the propulsor size was not scaled geometrically from the full scale to the wind-tunnel scale. Aerodynamic and aero-propulsive similarity between the wind-tunnel model and the full-scale aircraft were obtained by: 1) scaling the propulsor size such that the same ratio between the fan diameter and the fuselage momentum thickness at the fan location is achieved; and 2) optimizing the fan blades at the same operating conditions defined by the flow coefficient and load coefficient. The shroud geometry was also adapted from the full-scale CENTRELINE configuration to allow a tip gap of 0.75 mm, approximately corresponding to 1% of D_f. The shroud was equipped with 5 inlet and outlet vanes. The inlet vanes featured a NACA 0015 airfoil section with a rectangular planform. These vanes supported the shroud and were not optimized to de-swirl the flow. A more detailed discussion of the procedures and tools used in the fan design can be found in Ref. [25].

The unswept low wing (mean chord, c, of 165 mm, and planform area, S, of 0.216 m^2) featured a cambered airfoil, an aspect ratio of 8.46, a taper ratio of 0.4 and a linear washout of 2°. The vertical tail plane (VTP) featured a symmetric NACA 0012 airfoil, a taper ratio of 0.3 and a leading edge sweep angle of 30°.

Boundary layer transition was forced on all the surfaces through a 2.5 mm wide strips of 140 µm carborundum particles. The strips were placed on the fuselage, shroud, vertical tail and wing suction side at 5% of their respective lengths, and at 10% of the wing chord on the wing pressure side. Occurrence of transition was checked with microphone inspections of the boundary layer at all the operating conditions that were tested during the experiments.

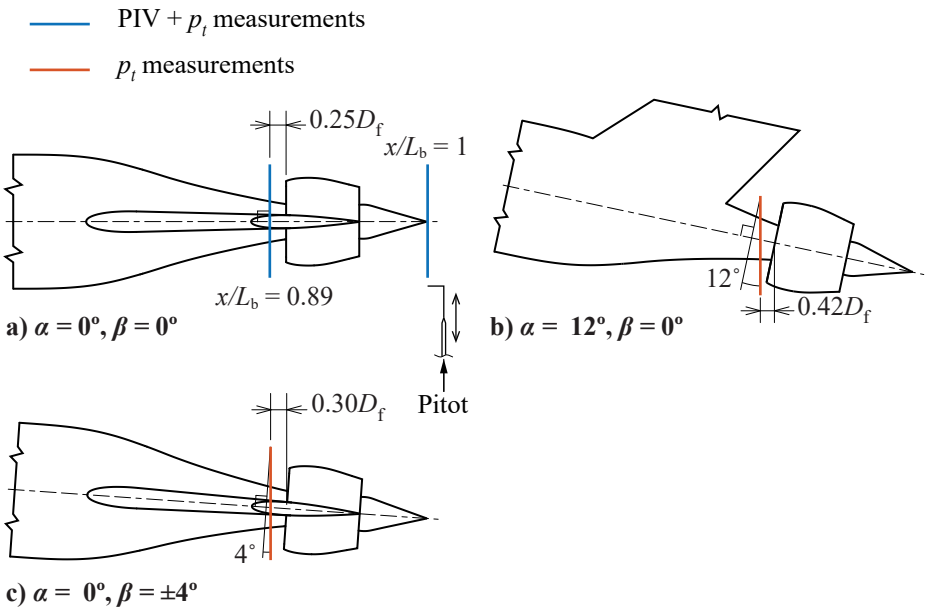

Fig. 6 Location and orientation of the PIV and total pressure measurements planes.

Table 1 Uncertainty values on the forces and moments coefficient measured through the external six-components balance.

	C_L	C_D	C_Y	$C_\mathcal{M}$	$C_\mathcal{N}$	$C_\mathcal{L}$
$\alpha = 0°$ $\beta = 0°$	0.0005	0.0002	0.0004	0.0009	0.0007	0.0009
$\alpha = 12°$ $\beta = 0°$	0.0025	0.0004	0.0006	0.0010	0.0007	0.0012

B. Measurement Techniques

1. Force and moments measurements

The aerodynamic forces and moments acting on the model were measured through the external six-components balance, to which the model was connected through the three supports. Only the model and the fuselage strut were sensed by the balance, since the wing struts were almost entirely covered by fairings bolted directly to the wind-tunnel wall (see Fig. 2). The balance readings were acquired for 15 s and time-averaged to filter the fluctuations due to turbulence, vibrations and other external factors. The non-dimensional force coefficients were defined using the freestream dynamic pressure, q_∞, and the wing planform area, S, as reference values. The uncertainty of the balance measurements was estimated from the deviation of repeated measurements. Tab. 1 reports the maximum absolute deviations from the mean measured for each force and moment coefficient for two different incidence settings.

2. Total pressure measurements

The total pressure distribution upstream and downstream of the fan inlet was measured with a L-shaped Pitot probe with an outer diameter of 0.6 mm. The probe was traversed in planes perpendicular to the freestream velocity direction with a variable spacing to account for the local gradients. The measurements were carried out both at cruise conditions ($\alpha = \beta = 0°$) and for non-zero angles of attack or sideslip. For the cases under sideslip, measurements at positive and negative β were combined to obtain the complete flowfield. Fig. 6 shows the position and orientations of the survey planes used for the different cases.

At each probe position, after a settling time of 2 s, the pressure data were recorded through an electronic pressure

Table 2 Main parameters of the Particle Image Velocimetry setup.

Imaging	
Focal length (mm)	105
Aperture	f/11
Digital resolution (px/mm)	12
Acquisition	
Pulse delay (µs)	30
Frequency (Hz)	10
Number of image pairs	500
Processing	
Interrogation window (px x px)	32 x 32
Overlap factor (%)	50
Spatial resolution (mm)	0.25
Uncertainty	
u uncertainty	$0.9\%V_\infty$
v uncertainty	$1.1\%V_\infty$
w uncertainty	$0.8\%V_\infty$
V uncertainty	$1.4\%V_\infty$

scanner for a period of 5 s and averaged over this period. Simultaneously, the freestream static and total pressures were measured with a Pitot static probe mounted at the inlet of the test section and acquired through the same pressure scanner. In this way, possible fluctuations in the freestream conditions due to temperature or velocity drifts could be accounted for. The raw total pressure measurements were used to define the non-dimensional total pressure coefficient: $C_{p_t} = (p_t - p_{t\infty})/q_\infty$.

3. Particle Image Velocimetry

Stereoscopic Particle Image Velocimetry (PIV) was employed to quantify the three velocity components in survey planes perpendicular to the freestream around the BLI propulsor for the cruise conditions ($\alpha = \beta = 0°$). The PIV planes coincided with the total pressure measurements planes which are sketched in Fig. 6a. The PIV system (laser, optics and cameras) were mounted on an electronic traversing system which was used to translate the measurement plane. Two LaVision© Imager sCMOS cameras (16-bit 2560 px × 2160 px) were used to record the particle images. The cameras were equipped with Nikon© AF Micro Nikkor 105 mm 1:2.8 D lenses set at an aperture of f/11 and mounted on LaVision© Scheimpflug adapter rings. A Quantel© Evergreen (double-pulse Nd:YAG, 200 mJ) laser and coated laser optics were used to generate the laser sheets with a thickness of around 2 mm. A Safex© Twin Fog smoke generator was used to seed the flow with Safex© Inside Nebelfluid. The seeding was injected downstream of the test section and spread uniformly in the entire flowfield within the wind-tunnel circuit. The image acquisition was controlled via a LaVision© Programmable Time Unit PTU X. The image pairs were recorded at a frequency of around 10 Hz and with a pulse delay of around 30 µs. For each case, a set of 500 phase-uncorrelated image pairs were acquired. The processing of the raw images was carried out in LaVision© Davis 8.4 using an iterative multi-pass correlation algorithm with a decreasing interrogation window size (from 96 px × 96 px for the first pass to 32 px × 32 px for the last pass, with an overlap factor of 50%). The uncertainty of the resulting velocity field was estimated directly at the correlation phase, using a statistical analysis of the correlation function implemented in Davis (see Ref.[26]). The main characteristics of the PIV measurements setup are summarized in Tab. 2.

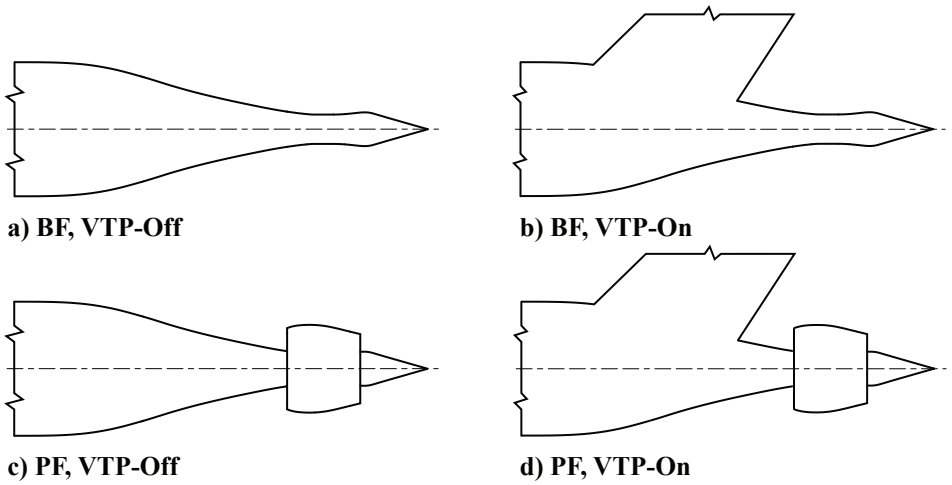

Fig. 7 Geometrical configurations tested in the wind-tunnel experiments.

C. Investigated cases

1. Geometric configuration

The modularity of the model allowed for the testing of four different geometric configurations, which are sketched in Fig. 7. In particular, the two main configurations were: a) the bare fuselage (BF), obtained by removing the BLI propulsor; b) the powered fuselage (PF), obtained by equipping the fuselage with the shrouded fan. For each of these configurations, the vertical tail plane could be installed (VTP-On) and disassembled (VTP-Off).

2. Flow and operating conditions

All the measurements were taken at a freestream velocity, V_∞, of 40 m/s, corresponding to a freestream Reynolds number based on the wing mean chord, Re_c, of around 460,000. At this freestream velocity, the freestream turbulence level is lower than 0.03% of V_∞ [27]. The angle of attack, α, was varied between $-6°$ and $12°$, while the angle of sideslip, β, was varied between $-8°$ and $8°$. Balance measurements were carried out in several conditions, including cases in which both α and β were varied together. Contrarily, other measurements were carried out in conditions obtained by varying one of the angles while the other was kept equal to zero. In addition, for the powered fuselage cases, the fan tip speed ratio, $U_{\text{tip}}/V_\infty = \frac{1}{2}\Omega D_{\text{f}}/V_\infty$, was varied by controlling the fan rotational speed, Ω.

D. Momentum and Energy Analysis

The momentum and energy components in the flowfield were analyzed through the Power Balance Method [4] based on the total pressure and stereoscopic PIV measurements. The momentum and energy flow rates across the survey planes were evaluated through the following definitions:

$$F_x = \iint \left[(p_t - p_{t\infty}) + \frac{1}{2}(u - V_\infty)^2 - \frac{1}{2}(v^2 + w^2) \right] \mathrm{d}S \tag{1}$$

$$\dot{E}_a = \iint \frac{1}{2}\rho u (u - V_\infty)^2 \mathrm{d}S \tag{2}$$

$$\dot{E}_v = \iint \frac{1}{2}\rho u (v^2 + w^2) \mathrm{d}S \tag{3}$$

$$\dot{E}_p = \iint (p - p_\infty)(u - V_\infty) \mathrm{d}S \tag{4}$$

where:

$$F_x : \text{is the axial momentum flow rate} \tag{5}$$

$$\dot{E}_a : \text{is the axial kinetic energy flow rate} \tag{6}$$

$$\dot{E}_v : \text{is the transverse kinetic energy flow rate} \tag{7}$$

$$\dot{E}_p : \text{is the pressure work rate} \tag{8}$$

and where:

$$u, v \text{ and } w : \text{are the Cartesian velocity components} \tag{9}$$

$$\rho : \text{is the density} \tag{10}$$

$$p_t : \text{is the total pressure} \tag{11}$$

$$p : \text{is the static pressure.} \tag{12}$$

The integrals were carried out over a circular survey plane, S, perpendicular to the freestream velocity direction and extending up to $r = 0.8R_b$. The momentum flow rate, F_x, is defined positive when corresponding to a momentum deficit and hence to a force component in the drag direction. In selected cases, to ease the interpretation of the results, F_a is defined as $F_a = -F_x$, and hence positive for a momentum excess and a force component in the thrust direction. The velocity components, u, v and w, were directly measured through the PIV measurements, while the total pressure, p_t, was obtained from the Pitot measurements. The effect of the probe incidence angle on the total pressure readings was corrected using the velocity data. For each probe position, the corresponding inflow angle was evaluated from the velocity field and used to correct the Pitot measurement through the probe calibration curve. The calibration curve was measured by placing the probe in the freestream flow and by tilting it with respect to the freestream velocity direction. Throughout the present analysis, the flow was assumed to be incompressible and hence $\rho = \rho_\infty$. The static pressure, p, was computed from the PIV and Pitot data through the incompressible Bernoulli's equation.

III. Results

The aerodynamic performance of the Propulsive Fuselage Concept, resulting from the complex aerodynamic interactions occurring between the BLI propulsor and the airframe was investigated through several measurement techniques. In this section, the main findings from the experimental study are presented and discussed. First, the effect of the BLI propulsor on the overall aircraft forces and moments is discussed. Subsequently, the flowfield around the BLI propulsor is investigated in detail. Finally, the distribution of the momentum and power components in the flowfield is presented. The results presented in this section are focussed on the aerodynamics of the powered fuselage (PF) configuration, while the performance of the bare fuselage (BF) configuration is discussed in the Appendix A.

A. Effect of BLI propulsor on aerodynamic forces and moments

The effect of the BLI propulsor on the overall aircraft aerodynamic forces and moments was quantified in different operating conditions through the six-components external balance. Fig. 8 presents the aerodynamic force and moment coefficients induced by the BLI propulsor as a function of the fan tip speed ratio, U_{tip}/V_∞. The propulsor-induced components were obtained by subtracting the values measured for the bare fuselage (BF) case from those measured for the powered fuselage (PF) case ($\Delta C_{()} = C^{\text{PF}}_{()} - C^{\text{BF}}_{()}$). These $\Delta C_{()}$ components account for the effects of the fan and of the shroud. The results of the balance measurements for the BF configuration are presented in Fig. 16 of the Appendix A. Fig. 8a reports the propulsor-induced lift, drag and pitching moment coefficients, respectively ΔC_L, ΔC_D, and $\Delta C_{\mathcal{M}}$, at $\beta = 0°$ and $\alpha = 0°$ and 12°. The measurements show that:

1) C_L is not affected by the propulsor installation and operating condition at $\alpha = 0°$. At $\alpha = 12°$, C_L slightly increases (up to 1% of C^{BF}_L) due to the lift produced by the shroud and the component of the fan thrust in the lift direction.
2) C_D changes significantly due to the propulsive unit installation. At $\alpha = 0°$, the added drag due to the shrouded fan was compensated by the propulsor at around $U_{\text{tip}}/V_\infty = 1$, at which $C^{\text{BF}}_D = C^{\text{PF}}_D$. The addition of the VTP contributes to the drag increase but it is not significantly influenced by the fan installation and settings. A consistent behavior is found at $\alpha = 12°$, although higher drag is measured relatively to the respective BF case at a given U_{tip}/V_∞. This is due to the higher drag produced by the shroud and to the composition of the thrust in the lift and drag directions.

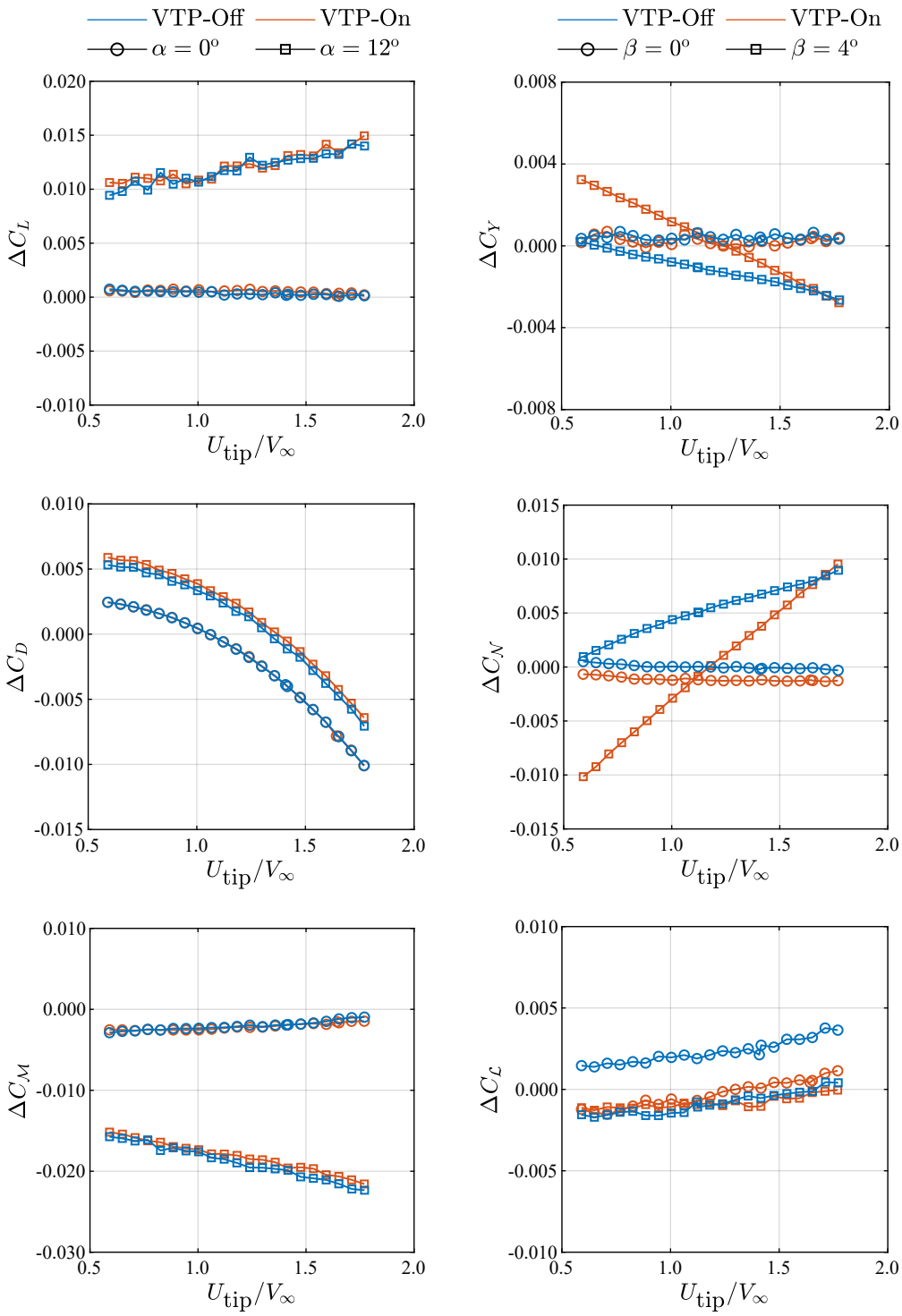

a) Longitudinal equilibrium ($\beta = 0^o$) **b) Lateral-directional equilibrium ($\alpha = 0^o$)**

Fig. 8 Effect of the BLI propulsor on the aerodynamic forces and moments coefficients. Balance measurements taken at $Re_c = 460,000$.

3) $C_{\mathcal{M}}$ is un-affected by the propulsor installation and setting at $\alpha = 0°$. However, at $\alpha = 12°$, the fan installation introduces a nose-down contribution to $C_{\mathcal{M}}$, due to the lift produced by the shroud contour and to the onset of an in-plane force component on the fan. The nose-down effect increases in magnitude for increasing U_{tip}/V_∞, suggesting that the fan in-plane force and the shroud lift increase at higher fan thrust settings.

Fig. 8b reports the propulsor-induced side force, yawing and rolling moment coefficients, respectively ΔC_Y, $\Delta C_{\mathcal{N}}$, and $\Delta C_{\mathcal{L}}$, at $\alpha = 0°$ and $\beta = 0°$ and 4°. The measurements show that:

1) ΔC_Y is small at $\beta = 0°$ due to the symmetric flow conditions and the effect of the fan is negligible. However, at $\beta = 4°$, C_Y slightly decreased (increased in magnitude) for increasing U_{tip}/V_∞, due to an increase in magnitude of the side force produced by the shroud and of the in-plane fan force. Comparing the VTP-Off and VTP-On data, it can be seen that the presence of the tail affected the side force produced by the propulsor unit which resulted in a change in slope of the ΔC_Y curve.
2) $\Delta C_{\mathcal{N}}$ shows a behavior which is consistent with that of ΔC_Y. $\Delta C_{\mathcal{N}}$ is small at $\beta = 0°$ and is not affected by the fan, due to the symmetric flow conditions. At $\beta = 4°$, the onset of the side force on the propulsor introduces a positive yawing moment contribution which increases with U_{tip}/V_∞. As noted for ΔC_Y, the interaction with the VTP results in an increased slope of the curve in the VTP-On case.
3) The effect of the fan installation and setting on $C_{\mathcal{L}}$ is negligible both at $\beta = 0°$ and $\beta = 4°$. The small increase seen in $\Delta C_{\mathcal{L}}$ at $\beta = 0°$ for increasing U_{tip}/V_∞ might be due to the increasing torque induced by the fan on the outlet vanes.

B. Distortions of the BLI propulsor inflow field

Fig. 9 shows the total pressure coefficient, C_{p_t}, measured upstream of the shroud inlet for the powered fuselage (PF) case at various incidence conditions. Moreover, for the cruise conditions ($\alpha = \beta = 0°$), both VTP-On and VTP-Off cases are shown. Fig. 9a and 9b show that in cruise conditions the fuselage boundary layer introduces total pressure gradients in the radial direction. In particular, at the survey plane location, the boundary layer thickness is approximately $0.65R_{\text{b}}$. In both VTP-Off and VTP-On cases, the bottom sector of the plot ($\phi > 120°$) is affected by the influence of the fuselage support strut. The vertical tail plane introduces a non-uniform p_t distribution which is due to two sources: the viscous wake of the tail, introducing a narrow and relatively strong p_t deficit (approximately for $-5° < \phi < 5°$), and the junction flow, introducing a wide and relatively weak p_t deficit close to the fuselage wall (approximately for $-30° < \phi < 30°$).

The inflow total pressure was measured at $\alpha = 12°$ and $\beta = 0°$ to simulate conditions representative of take-off or top-of-climb maneuvers. Fig. 9c shows the p_t distribution for the PF, VTP-On case. The increased incidence angle results in the onset of a cross-flow around the fuselage section (see for example Ref. [28, 29]). This cross-flow displaces the lower p_t flow farther from the fuselage on the leeward (upper) side, while higher p_t flow is entrained on the windward (bottom) side. The VTP causes a p_t deficit due to its viscous wake similarly to the $\alpha = 0°$ case. However, the junction flow distortion is not clearly visible anymore close to the fuselage contour. This could be a consequence of the cross-flow component that displaces the horseshoe vortex further from the surface.

Fig. 9d reports the fan-inflow total pressure for $\alpha = 0°$ and $\beta = 4°$ for the PF, VTP-On case. Similarly to the case at $\alpha = 12°$, due to the cross-flow component around the fuselage contour, the low momentum fluid is displaced on the leeward (left-hand) side while higher p_t flow is entrained on the windward (right-hand) side. Moreover, the vertical tail produces a strong asymmetric distortion which is enhanced by the fact that the tail is producing lift under the sideslip β. In particular, a low p_t region is found on the leeward side (corresponding to the suction side of the vertical tail) in proximity of the fuselage body, presumably due to trailing edge separation. In fact, inside the fuselage boundary layer, the effective incidence angle of the tail sections are most likely higher than the sideslip angle, due to the lower axial velocity component. On the windward side (corresponding to the pressure side of the vertical tail), the p_t distribution typical of an horseshoe vortex can be identified, as a result of the junction flow developing at the tail-fuselage intersection. Consequently, strong pressure gradients are found in the azimuthal direction around $\phi = 0°$.

The total pressure distribution at the fan inlet found in cruise conditions, displayed in Fig. 9b, was decomposed in the three basic components associated to the fundamental aerodynamic phenomena that cause them, namely: the fuselage boundary layer, the VTP wake and the junction flow. The results of the decomposition are reported in Fig. 10. Note that the total pressure measurements were done only for $-18° \leq \phi \geq 198°$ and then mirrored for visualization purposes. Moreover, the distortions induced by each of these distortion components were summarized through the standard distortion parameters DC(60), CDI and RDI, and are gathered in Tab. 3. The parameters were defined as (see Ref. [30]):

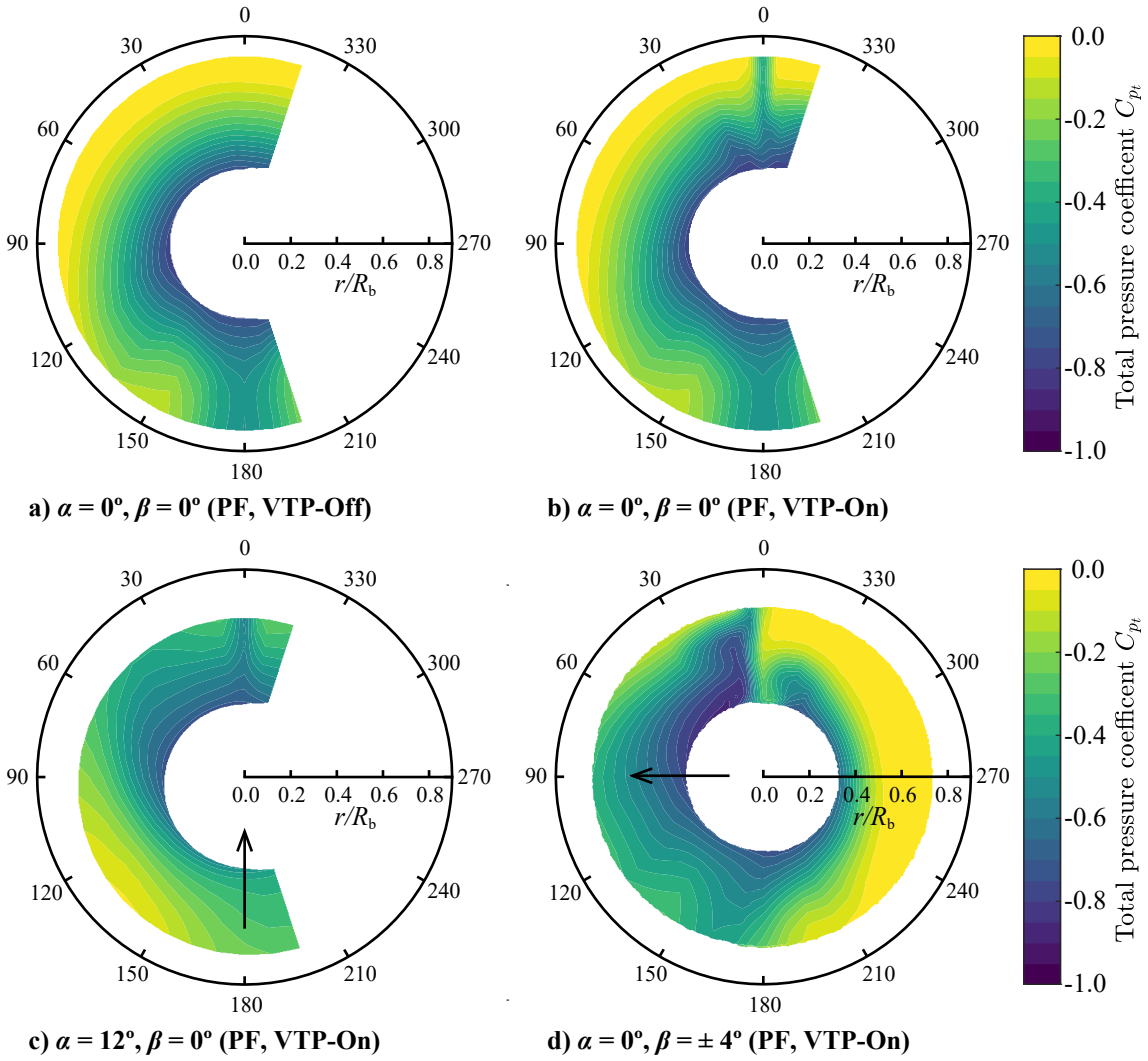

a) $\alpha = 0^o, \beta = 0^o$ **(PF, VTP-Off)**

b) $\alpha = 0^o, \beta = 0^o$ **(PF, VTP-On)**

c) $\alpha = 12^o, \beta = 0^o$ **(PF, VTP-On)**

d) $\alpha = 0^o, \beta = \pm 4^o$ **(PF, VTP-On)**

Fig. 9 Total pressure distributions upstream of the BLI propulsor for the powered fuselage (PF) case at various incidence angles (back view). Arrows indicate the direction of the crossflow component. Total pressure measurements taken at $Re_c = 460,000$ and $U_{tip}/V_\infty = 1.7$.

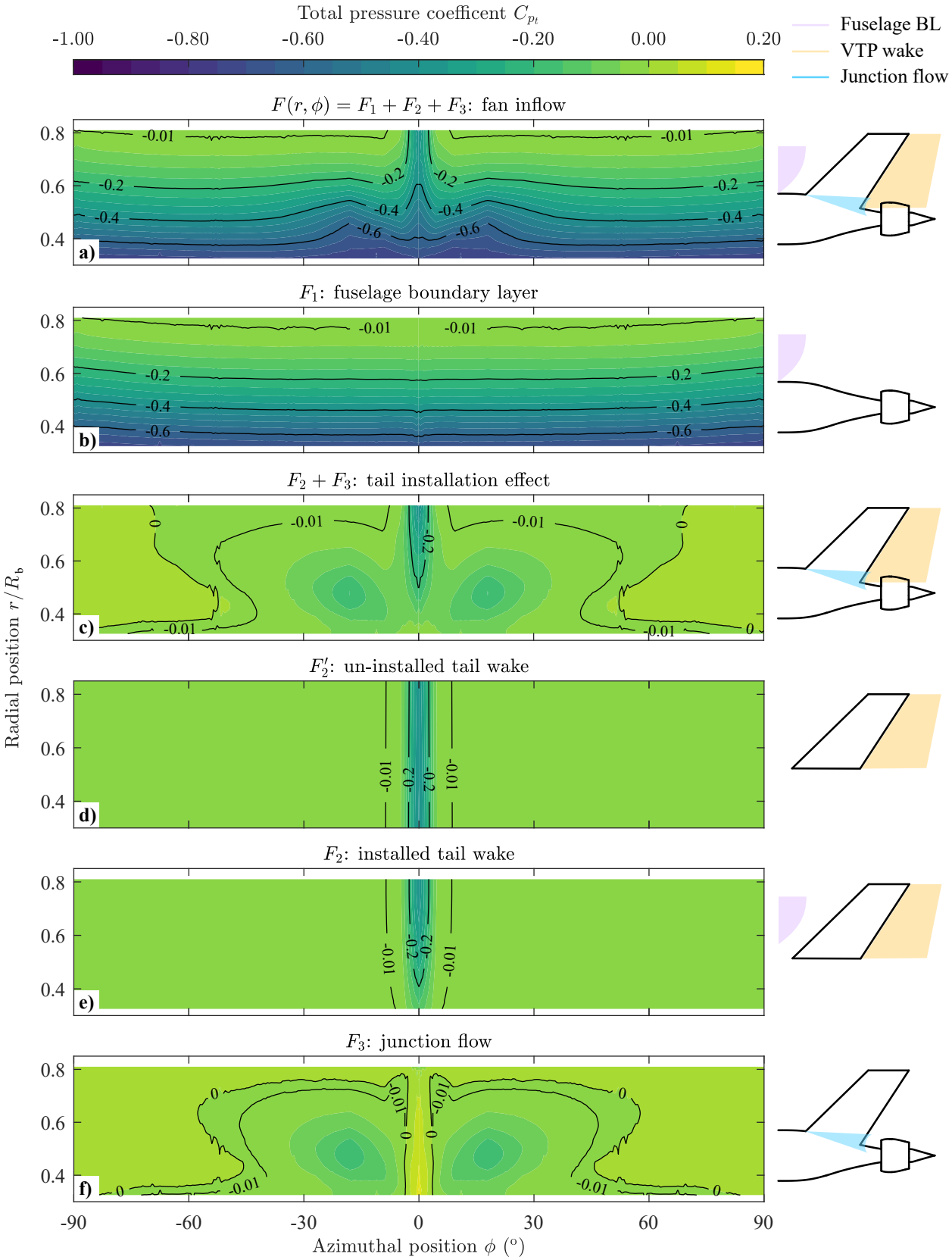

Fig. 10 Fundamental components of the fan inflow total pressure distribution in cruise conditions. Total pressure measurements taken at $\alpha = 0° = \beta = 0°$, U_{tip}/V_∞ and $Re_c = 460,000$.

$$\mathrm{DC}(60) = \frac{p_t^{\mathrm{avg}} - p_{t,60^\circ}^{\mathrm{avg}}}{p_t^{\mathrm{avg}}} \tag{13}$$

$$\mathrm{CDI} = \max_r \left(\frac{p_t^{\mathrm{avg}}(r) - p_t^{\mathrm{min}}(r)}{p_t^{\mathrm{avg}}} \right) \tag{14}$$

$$\mathrm{RDI} = \max \left(\frac{p_t^{\mathrm{avg}} - p_t^{\mathrm{avg}}(r_{\mathrm{min}})}{p_t^{\mathrm{avg}}}, \frac{p_t^{\mathrm{avg}} - p_t^{\mathrm{avg}}(r_{\mathrm{max}})}{p_t^{\mathrm{avg}}} \right) \tag{15}$$

where:

p_t^{avg} : is the average total pressure value in the survey plane (360°)
$p_{t,60^\circ}^{\mathrm{avg}}$: is the minimum average total pressure value in a sector of 60°
$p_t^{\mathrm{avg}}(r)$: is the average total pressure value at the radial position r
$p_t^{\mathrm{min}}(r)$: is the minimum total pressure value at the radial position r

The momentum distribution, C_{p_t}, shown in Fig. 10a, is primarily the result of the flow around the fuselage, vertical tail and their mutual interaction and is a function of both r and ϕ, i.e. $C_{p_t} = F(r, \phi)$.

F_1, shown in Fig. 10b, represents the momentum deficit due to the fuselage boundary layer and it was directly measured on the VTP Off configuration. Ideally, for an axisymmetric fuselage at zero incidence, and neglecting the effect of the wings, F_1 would be a function of r and constant with ϕ. In practice, due to the lifting wings and the interference of the fuselage support strut, the measured F_1 deviates from an axisymmetric condition.

Furthermore, the total pressure distribution component due to the tail installation was isolated by subtracting the VTP-On and VTP-Off cases and it is reported in Fig. 10c. This component can be further decomposed in two parts: F_2, representing the viscous wake of the VTP, and F_3, representing the effect of the tail-fuselage junction flow. To obtain F_2, firstly the un-installed tail wake, F_2', reported in Fig. 10d, was estimated. F_2' represents the momentum deficit distribution in the wake of the VTP operating in uniform freestream flow (hence without the effect of the fuselage boundary layer). F_2' was estimated by assuming a C_{p_t} profile equal in shape to the profile that was measured outside of the fuselage boundary layer ($r/R_{\mathrm{b}} = 0.795$). At each radial position r, this C_{p_t} profile was scaled proportionally to the local VTP chord length. This is valid in the assumption that the section drag scales linearly with the section chord length. Subsequently, the installed tail wake, F_2, reported in Fig. 10e, was obtained by scaling F_2' with the local total pressure ratio, $p_t/p_{t\infty}$, in order to take into account the non-uniform dynamic pressure impinging on the different VTP sections. This is valid in the assumption that radial static pressure gradients can be neglected in the fuselage boundary layer. F_2 results in a p_t deficit concentrated around the center of the VTP ($-5^\circ < \phi < 5^\circ$) and non-linearly decreasing in intensity toward the fuselage wall. Finally, F_3, reported in Fig. 10f, was obtained as complementary of F_2 to the total tail installation effect. F_3 is strongly two-dimensional and characterized by a low total pressure region coincident with the core of the horse-shoe vortex.

The decomposition of C_{p_t} clearly shows that the total momentum deficit characterizing the BLI fan inflow can be obtained as a combination of elementary components associated with well-defined physical sources of momentum deficit. Comparing the different elements, it can be concluded that the lowest p_t values are induced by the fuselage boundary layer (Fig. 10b). However, since this deficit is approximately axisymmetric, it does not induce non-uniform disk loads and the design of the BLI propulsor can be adapted to sustain the distortion with minor performance penalties (see for example Ref. [13]). On the contrary, the inlet distortions induced by the tail installation will induce non-uniform disk loads and hence potentially affect the aero-acoustic and aero-mechanical performance of the BLI fan [19, 20]. This qualitative analysis is supported by the distortion parameters reported in Tab. 3. In fact, it can be observed that the momentum deficit due to the fuselage boundary layer, F_1, contributes with the highest RDI coefficient, while the VPT wake, F_2, is characterized by the highest CDI coefficient. Overall, the DC(60) values measured are relatively low due to the fact that the axysimmetric component of the inlet distortions (F_1) is dominant and the strongest non-axysimmetric component of the distortions (F_2) is concentrated in a narrow sector.

Stereoscopic PIV measurements were carried out in a plane perpendicular to the freestream direction at $x/L_{\mathrm{b}} = 0.89$ to quantify the velocity field at the shroud inlet in cruise conditions (see Sec. II.B.3). Fig. 11 reports the three velocity components, u, v, and w, together with the swirl angle, θ, and the axial vorticity component, ω_x, for the BF, VTP-On configuration.

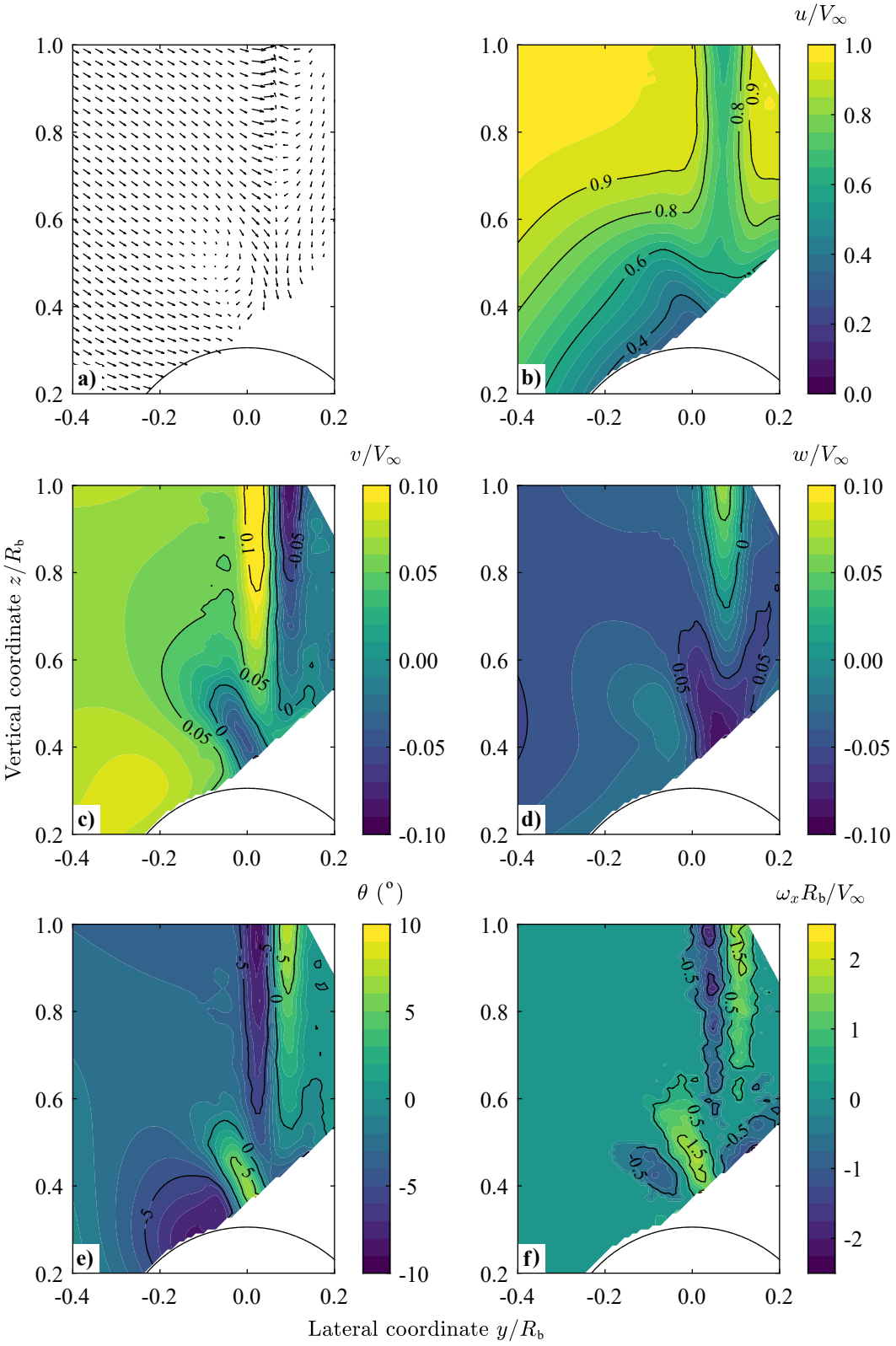

Fig. 11 Flowfield at $x/L_b = 0.89$ for the BF, VTP-On configuration (back view). Stereoscopic PIV measurements for $\alpha = 0° = \beta = 0°$ and $Re_c = 460,000$.

Table 3 Inlet distortion metrics for the fundamental components of the fan inflow total pressure distribution in cruise conditions (F: fan inflow; F_1: fuselage boundary layer; F_2: installed tail wake; F_3: junction flow). Total pressure measurements taken at $\alpha = 0° = \beta = 0°$, U_{tip}/V_∞ and $Re_c = 460,000$.

	F	F_1	F_2	F_3
DC(60)	0.06	0.03	0.02	0.04
CDI	0.85	0.10	0.39	0.20
RDI	0.66	0.63	0.01	0.01

Fig. 11b displays the axial velocity contour which, similarly to the C_{p_t} in Fig. 9b, is characterized by the fuselage boundary layer, VTP wake and junction flow. The VTP influences the fan inflow field with in-plane velocity components, which can be easily visualized in Fig. 11a. In fact, in the VPT wake, the lateral velocity component, v, is directed toward the center of the wake itself (Fig. 11c) due to the wake contraction. Moreover, a positive vertical (spanwise) velocity component, w, is found (Fig. 11d). This vertical flow, directed from the root to the tip of the tail, is due to the onset of a crossflow component in the tail boundary layer induced by the leading edge sweep. These v and w distributions have two direct consequences on the fan inflow. First, downstream of the tail plane, a velocity tangent to the fan plane is induced, which is co-rotating with the blades on the approaching-blade side (in this case left-hand side) and counter-rotating on the retreating-blade side (in this case right-hand case). This results in a swirl angle, θ, displayed in Fig. 11e, peaking at around $\pm 8°$ in the VPT wake. Second, the vertical crossflow in the VTP boundary layer introduces streamwise vorticity ω_x that is transported downstream and ingested by the fan (Fig. 11f).

C. Flowfield downstream of the BLI propulsor

The flowfield downstream of the BLI propulsor was quantified through total pressure and stereoscopic PIV measurements on a survey plane perpendicular to the freestream velocity direction located at the fuselage trailing edge (plane at $x/L_b = 1$ of Fig. 6). The measurements were carried out at $\alpha = \beta = 0°$ and at $U_{tip}/V_\infty = 1.7$. The distributions of total pressure, p_t, axial velocity velocity, u, tangential velocity, v_t, and axial vorticity, ω_x, are reported in Fig. 12.

The fan slipstream clearly shows a total pressure and axial velocity higher than the freestream (Fig. 12a and Fig. 12b, respectively). The low total pressure and velocity region around the fuselage axis is due to the onset of a vortical structure around the fuselage hub. This structure, induced by the fan slipstream, was analyzed in detail in a previous related work [16]. Furthermore, C_{p_t} and u show a non-axisymmetric distribution over the entire slipstream annulus. In particular, the wakes of the outlet vanes (see Fig. 13) are visible as they are characterized by a relatively lower total pressure and axial velocity.

Moreover, the outer region of the slipstream is affected by the presence of streamwise vortices (Fig. 12d) which induce the structures labeled as A and B in Fig. 12. These vortices are thought to be due to the interactions between the shroud-vanes junction flow and the fan slipstream, as sketched in Fig. 13. The horseshoe vortex generated at the intersection between the outlet and inlet vanes and the shroud results in five pairs of counter-rotating vortices, corresponding to the vortices A and B respectively. These vortices are convected downstream in the fan slipstream, hence following an helical trajectory. The viscous interaction with the swirling flow in the fan slipstream results in an enhanced dissipation of the co-rotating ($+\Gamma$) filament while keeping the counter-rotating filament ($-\Gamma$) stable. It must be noted that, though consistent with the experimental observations, no experimental data are available to directly validate the proposed phenomena. A more detailed investigation of the flowfield is required through dedicated measurements of numerical analysis, possibly with time-resolved flow data.

Finally, the tangential velocity component, v_t (Fig. 12c), has a uniform distribution in the center of the fan slipstream and strongly increases toward the hub region due to the presence of the hub vortex.

D. Flow Momentum and Power Analysis

The total pressure and velocity data were combined to estimate the main momentum and power fluxes across a survey plane perpendicular to the flow and positioned at $x/L_b = 0.89$ and at $x/L_b = 1$ for the BF and PF configurations. The terminology, main equations and procedures used are discussed in Sec. II.D. Fig. 14 reports the distribution of the momentum and power flux densities in the survey planes. The fluxes, dF_a, $d\dot{E}_a$, $d\dot{E}_v$, and $d\dot{E}_p$, represent the amount of momentum or power transported through the survey plane per unit area and their surface integral is equal to the

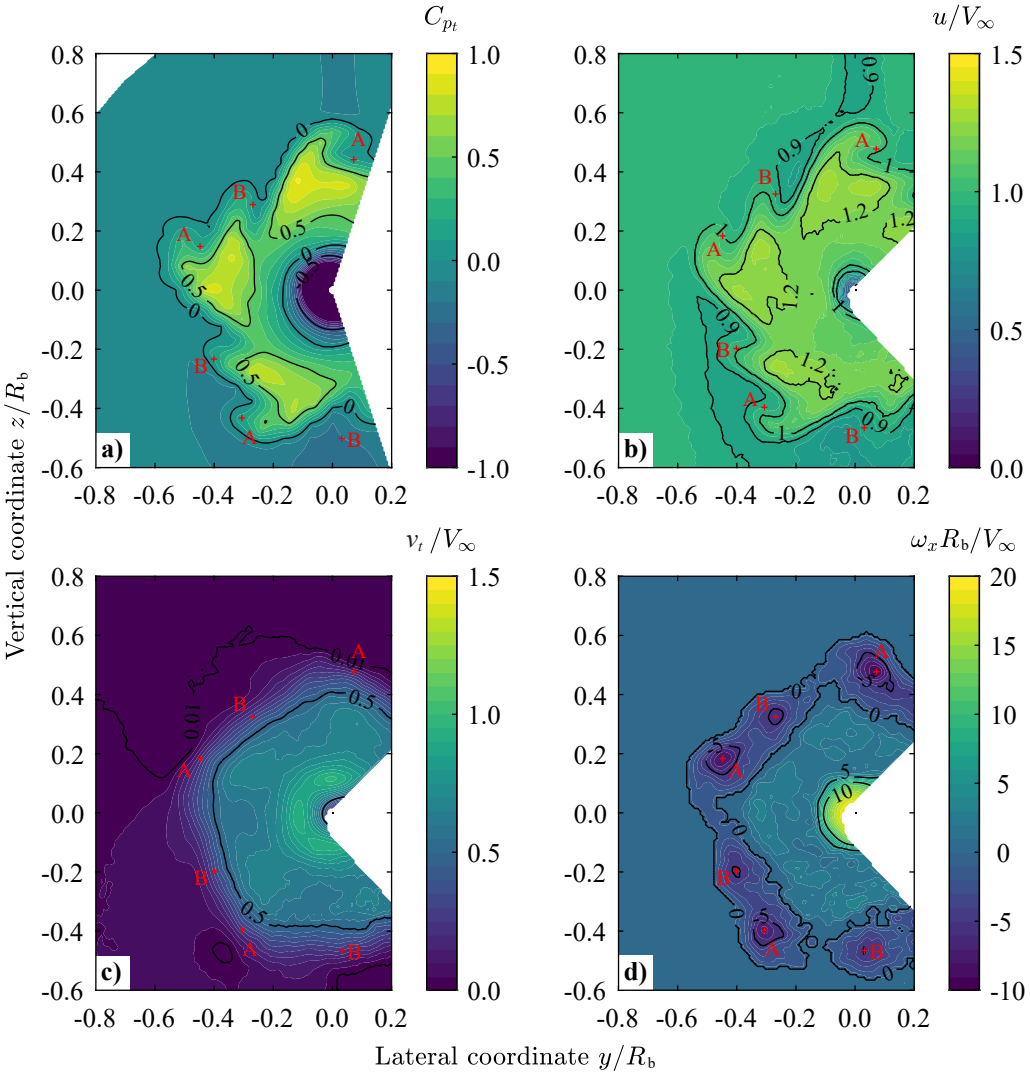

Fig. 12 Flowfield at $x/L_b = 1$ for the PF, VTP-On configuration (back view). Total pressure and stereoscopic PIV measurements for $\alpha = 0° = \beta = 0°$, $U_{tip}/V_\infty = 1.7$ and $Re_c = 460,000$.

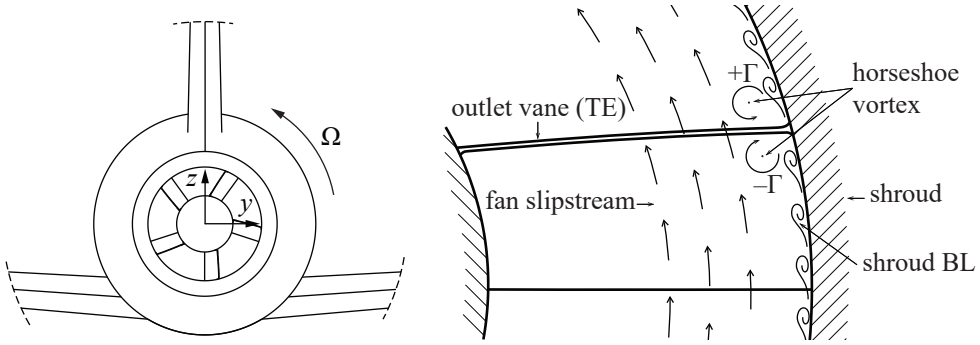

Fig. 13 Schematic of the flow interactions between the fan slipstream and the viscous flow around the vane and shroud surfaces.

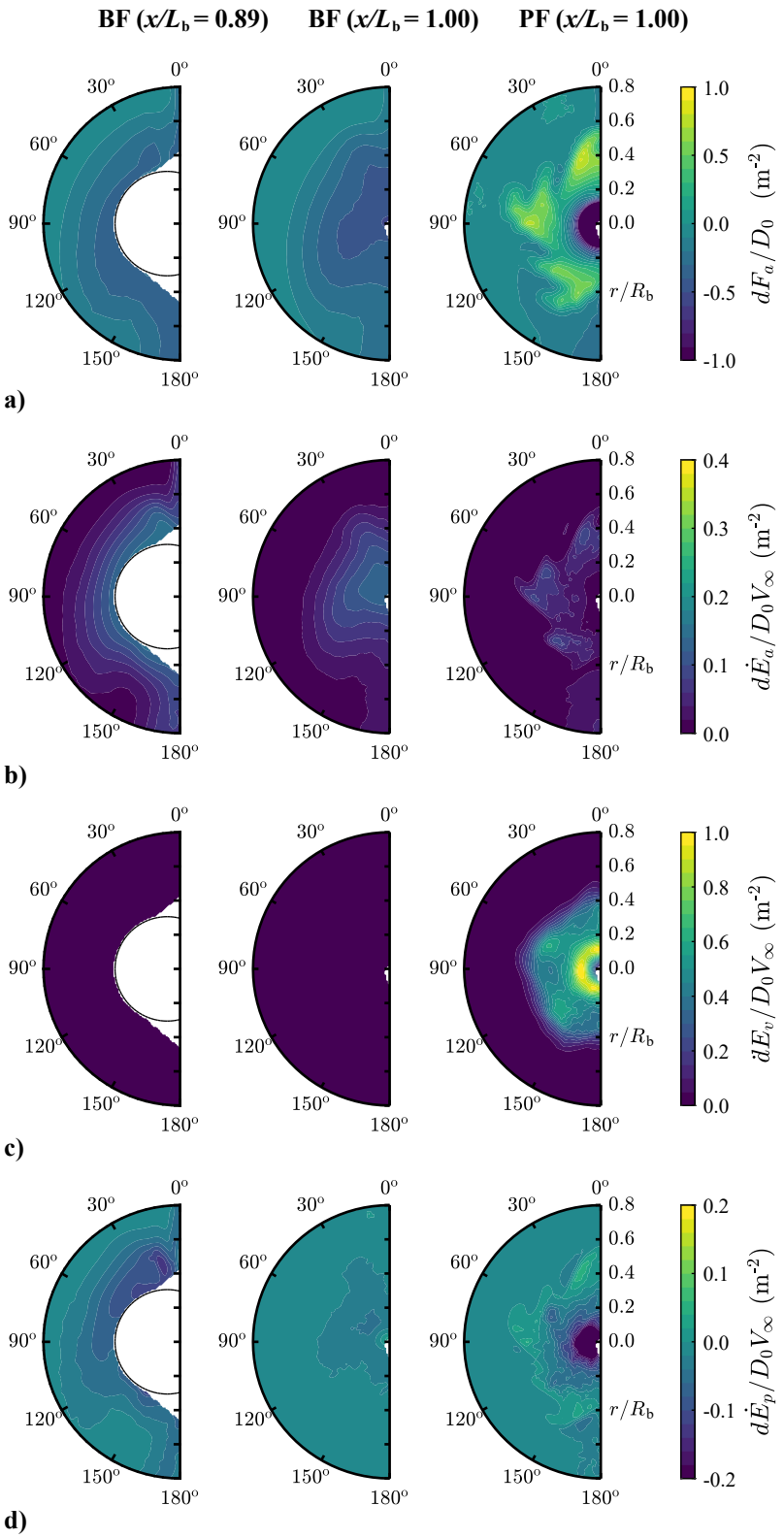

Fig. 14 Distributions of the momentum and energy flux densities at $x/L_b = 0.89$ and $x/L_b = 1.00$ for the BF, VTP-On and PF, VTP-On cases (back view). Total pressure and stereoscopic PIV Measurements for $\alpha = 0° = \beta = 0°$, $U_{tip}/V_\infty = 1.7$ (PF case) and $Re_c = 460,000$.

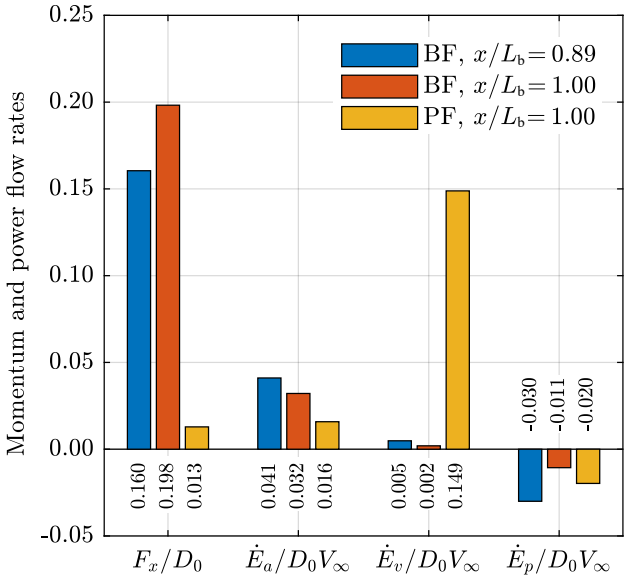

Fig. 15 Integral momentum and energy flow rates at $x/L_b = 0.89$ and $x/L_b = 1.00$ for different fuselage configurations. Measurements for $\alpha = 0° = \beta = 0°$.

respective flow rates, F_x, $\dot{E}_a$, $\dot{E}_v$, $\dot{E}_p$, defined in Sec. II.D. The momentum and power flux densities were expressed as ratio to D_0 and D_0V_∞, respectively, where D_0 is the measured drag of the BF, VTP-On case at $\alpha = \beta = 0°$. Therefore, the momentum and power terms were related to a reference drag and drag power associated to the baseline aircraft configuration. In particular, in the calculation of D_0 the drag of the fuselage strut was estimated through a 2-D viscous flow solver (`XFOIL`, Ref. [31]) and subtracted from the balance measurements.

Fig.14a shows the momentum flux density, $dF_a = -dF_x$, which is positive for a local momentum excess and negative for a local momentum deficit. Clearly, for the BF cases, dF_a shows a momentum deficit in the fuselage boundary layer and in the wake of the VTP on both survey planes. For the PF configuration, a momentum excess is found in the fan slipstream while a strong momentum deficit is measured around the fuselage axis due to the onset of the vortical flow already discussed. Similarly, the axial kinetic energy flux density, $d\dot{E}_a$ in Fig. 14b, shows that for the BF case the kinetic energy flux is concentrated in the regions of momentum deficit (i.e. the fuselage boundary layer and the VTP wake). However, for the PF case, $d\dot{E}_a$ shows relatively low values thanks to the axial velocity induced by the BLI fan. Contrarily, as shown in Fig. 14c, the transverse kinetic energy flux density, $d\dot{E}_v$, is relatively low for the BF cases. For the PF case, the swirl velocity induced by the fan resulted in a strong $d\dot{E}_v$, which reaches the maximum values in the vortical flow region around the fuselage axis. Finally, the pressure work flux, $d\dot{E}_p$ in Fig. 14d, shows that for the BF case the flow is expanded in the fuselage boundary layer at $x/L_b = 0.89$ and that the static pressure recovers substantially already at $x/L_b = 1$. For the PF case, the static pressure slightly exceeds the freestream value in the fan slipstream while very low pressure is found the vortical structure around the fuselage axis.

Fig. 15 reports the momentum and energy flow rates obtained as surface integrals of the flux densities discussed above. As already discussed, the momentum and power terms are expressed in terms of D_0 and D_0V_∞. It can be seen that for the BF case at $x/L_b = 0.89$ a momentum flow rate equal to approximately 16% of the total aircraft drag was measured in the survey plane. Moreover, F_x increased to almost 20% of D_0 at $x/L_b = 1$. This suggests that a substantial share of momentum in the fuselage boundary layer (around 20-25%), associated to the fuselage body drag, is dissipated in the flow around the contracting aft-cone of the fuselage body. This shows very good consistency with the results of a related study focussed on the study of the same fuselage geometry in a 2-D axisymmetric setup [16].

The kinetic energy flow rate, $\dot{E}_a$, shows an opposite variation when moving from $x/L_b = 0.89$ to $x/L_b = 1$ for the BF case, resulting in around 25% lower flow rate at the trailing edge. This is due to the contributions to $\dot{E}_a$ found in the wakes of the VTP and of the fuselage support strut which are clearly visible at $x/L_b = 0.89$ and are much weaker at $x/L_b = 1$. In fact, the results of a previous related work (Ref. [16]) have shown that, for the same fuselage geometry without the VTP and the fuselage strut, $\dot{E}_a$, has a similar value at $x/L_b = 0.89$ and $x/L_b = 1$. For the PF case, the value of $\dot{E}_a$ was effectively reduced of around 50% at $x/L_b = 1$ compared to the BF case. The analysis of $\dot{E}_a$ shows that: first, around 3-4% of the total aircraft drag power, D_0V_∞, is transported and dissipated in the wake of the aircraft; this values

represent the ideal power benefit that could be achieved with a so-called ideal BLI propulsor (see Ref. [4]). Moreover, the acceleration imposed by the BLI fan on the low-momentum fuselage boundary layer effectively reduces $\dot{E}_a$ and hence the wake dissipation.

The transverse kinetic energy flow rate, $\dot{E}_v$, shows very small values for the BF cases, due to the relatively small in-plane velocity components. On the contrary, $\dot{E}_v$ is the dominant factor for the PF case, due to the relatively strong swirl component in the fan slipstream. This component can be mitigated with an accurate design of the outlet vanes to recover the swirl velocity induced by the fan stage. Finally, the pressure work rate, $\dot{E}_p$, shows a negative value for the BF cases, due to the fact that the flow accelerates (decreasing pressure) due to the fuselage curvature. The expanded flow then undergoes a compression (increasing pressure) around the contracting aft-cone toward the trailing edge and the associated pressure recovery results in a decreasing (in magnitude) pressure work rate at $x/L_\mathrm{b} = 1$. The decrease in $\dot{E}_p$ for the PF case due to the BLI fan is due to the low static pressure found in the core of the vortical flow around the fuselage axis (see again Fig. 14d).

IV. Summary & Conclusions

This paper has presented an experimental analysis of an aircraft featuring a fuselage-mounted boundary-layer ingesting propulsor representative of the CENTRELINE Propulsive Fuselage Concept. The wind-tunnel tests were carried out in the low-speed wind-tunnel facilities of Delft University of Technology.

The goals of the experiment were:

1) To study the effect of the fuselage-mounted BLI propulsor on the overall-aircraft aerodynamic forces and moments in all flight conditions.
2) To characterize the flowfield around the BLI propulsor and the aerodynamic interactions occurring between the propulsor and the airframe.

The analysis of the experimental data shows that:

1) In cruise conditions ($\alpha = \beta = 0°$), the effect of the BLI propulsor on the aircraft forces and moments are mostly limited to the thrust–drag equilibrium. However, at incidence, the BLI propulsor showed a non-negligible effect on both longitudinal and lateral-directional equilibrium.
2) In cruise conditions, the fuselage boundary layer represents the strongest distortion to the fan inflow while the influence of the wing lift and downwash is secondary. The vertical tail plane (VTP) introduces a total pressure deficit which can be decomposed in two contributions: the VTP viscous wake, with a restricted azimuthal extension ($-5° < \phi < 5°$), and the horseshoe vortex structure that develops at the fuselage-tail junction. The VTP wake induces in-plane velocity components, associated with the wake contraction and spanwise crossflow, which create non-negligible swirl at the BLI propulsor inlet.
3) In off-design conditions (α, $\beta \neq 0°$), the crossflow component around the fuselage contour introduces a non-axisymmetric distortion characterized by low total pressure on the leeward side and high total pressure on the windward side. At $\beta = 4°$, the vertical tail strongly affects the inflow field as it produces lift under the sideslip. The associated total pressure distortion is characterized by sharp gradients in the azimuthal and radial directions.
4) The BLI propulsor strongly alters the flow around the fuselage aft-section. The flowfield is characterized by regions of relatively high momentum (fan slipstream) and low momentum (hub vortex).
5) An axial momentum flow rate equal to 16% and 20% of the total aircraft drag was estimated at $x/L = 0.89$ and $x/L = 1$, respectively, which represent the drag force associated to the fuselage body and VTP root section. Moreover, the axial kinetic energy flow rate, $\dot{E}_a$, varied from 4% to 3% of the aircraft drag power, $D_0 V_\infty$, across the same planes. This indicates that a power saving of around 3-4% could be achieved through an ideal BLI propulsor.
6) The axial momentum and kinetic energy flow rates at the fuselage trailing edge are substantially reduced by the BLI propulsor, suggesting that the acceleration induced on the boundary layer flow by the BLI propulsor effectively decreases $\dot{E}_a$ and hence the dissipation occurring in the aircraft wake.

Acknowledgments

This work was conducted within the CENTRELINE project, which has received funding from the European Union's Horizon 2020 research and innovation programme under Grant Agreement No. 723242. The authors wish to express their gratitude to Nando van Arnhem, Daniele Ragni, Tomas Sinnige, Reynard de Vries and Sumit Tambe for their contribution to the design, execution and analysis of the wind-tunnel experiments.

References

[1] Wislicenus, G., "Hydrodynamics and Propulsion of Submerged Bodies," *ARS Journal*, Vol. 30, No. 12, 1960, pp. 1140–1148. https://doi.org/10.2514/8.5351.

[2] Gearhart, W., and Henderson, R., "Selection of a Propulsor for a Submersible System," *Journal of Aircraft*, Vol. 3, No. 1, 1966, pp. 84–90. https://doi.org/10.2514/3.59270.

[3] Smith, L. H., "Wake ingestion propulsion benefit," *AIAA Journal of Propulsion and Power*, Vol. 9, No. 1, 1993, pp. 74–82. https://doi.org/10.2514/3.11487.

[4] Drela, M., "Power Balance in Aerodynamic Flows," *AIAA Journal*, Vol. 47, No. 7, 2009, pp. 1761–1771. https://doi.org/10.2514/1.42409.

[5] Lv, P., Gangoli Rao, A., Ragni, D., and Veldhuis, L., "Performance Analysis of Wake and Boundary-Layer Ingestion for Aircraft Design," *Journal of Aircraft*, Vol. 53, No. 5, 2016, pp. 1517–1526. https://doi.org/10.2514/1.C033395.

[6] Arntz, A., and Atinault, O., "Exergy-Based Performance Assessment of a Blended Wing–Body with Boundary-Layer Ingestion," *AIAA Journal*, Vol. 53, No. 12, 2015, pp. 3766–3776. https://doi.org/10.2514/1.J054072.

[7] Uranga, A., Drela, M., Greitzer, E. M., Hall, D. K., Titchener, N. A., Lieu, M. K., Siu, N. M., Casses, C., Huang, A. C., Gatlin, G. M., et al., "Boundary Layer Ingestion Benefit of the D8 Transport Aircraft," *AIAA Journal*, 2017, pp. 1–17.

[8] Wiart, L., Atinault, O., Boniface, J.-C., and Barrier, R., "Aeropropulsive Performance Analysis of the NOVA Configurations," *30th Congress of the International Council of the Aeronautical Sciences*, 2016.

[9] Steiner, H.-J., Seitz, A., Wieczorek, K., Plötner, K., Isikveren, A. T., and Hornung, M., "Multi-disciplinary design and feasibility study of distributed propulsion systems," *28th International Congress of the Aeronautical Sciences*, 2012, pp. 23–28.

[10] Welstead, J., and Felder, J. L., "Conceptual design of a single-aisle turboelectric commercial transport with fuselage boundary layer ingestion," *54th AIAA Aerospace Sciences Meeting*, 2016, p. 1027. https://doi.org/10.2514/6.2016-1027.

[11] Seitz, A., Habermann, A. L., Peter, F., Troeltsch, F., Castillo Pardo, A., Della Corte, B., van Sluis, M., Goraj, Z., Kowalski, M., Zhao, X., Grönstedt, T., Bijewitz, J., and Wortmann, G., "Proof of Concept Study for Fuselage Boundary Layer Ingesting Propulsion," *Aerospace*, Vol. 8, No. 1, 2021, pp. 1–16. https://doi.org/10.3390/aerospace8010016.

[12] Isikveren, A. T., Seitz, A., Bijewitz, J., Mirzoyan, A., Isyanov, A., Grenon, R., Atinault, O., Godard, J. L., and Stückl, S., "Distributed Populsion and Ultra-High By-Pass Rotor Study at Aircraft Level," *Aeronautical Journal*, Vol. 119, No. 1221, 2015, pp. 1327–1376. https://doi.org/10.1017/S0001924000011295.

[13] Castillo Pardo, A., and Hall, C. A., "Aerodynamics of Boundary Layer Ingesting Fuselage Fans," *ASME Journal of Turbomachinery*, Vol. 143, No. 4, 2021, pp. 1–9. https://doi.org/10.1115/1.4049918.

[14] Seitz, A., Habermann, A. L., and van Sluis, M., "Optimality Considerations for Propulsive Fuselage Power Savings," *Journal of Aerospace Engineering*, 2020. https://doi.org/10.1177/0954410020916319.

[15] van Sluis, M., Della Corte, B., and Gangoli Rao, A., "Aerodynamic Design Space Exploration of a Fuselage Boundary Layer Ingesting Aircraft Concept," Manuscript in preparation.

[16] Della Corte, B., van Sluis, M., Gangoli Rao, A., and Veldhuis, L., "Power Balance Analysis Experiments on an Axisymmetric Fuselage with an Integrated Boundary-Layer-Ingesting Fan," *AIAA Journal*, Manuscript accepted.

[17] Gunn, E. J., and Hall, C. A., "Non-Axisymmetric Stator Design for Boundary Layer Ingesting Fans," *ASME Turbo Expo*, 2017. https://doi.org/10.1115/GT2017-63082.

[18] Hall, D. K., Greitzer, E. M., and Tan, C. S., "Analysis of Fan Stage Design Attributes for Boundary Layer Ingestion," *ASME Turbo Expo*, 2016. https://doi.org/10.1115/GT2016-57808.

[19] Mårtensson, H., "Harmonic Forcing from Distortion in a Boundary Layer Ingesting Fan," *Aerospace*, Vol. 8, No. 3, 2021, pp. 1–13. https://doi.org/10.3390/aerospace8030058.

[20] Petrosino, F., Barbarino, M., and Staggat, M., "Aeroacoustics Assessment of an Hybrid Aircraft Configuration with Rear-Mounted Boundary Layer Ingested Engine," *Applied Sciences*, Vol. 11, No. 7, 2021. https://doi.org/10.3390/app11072936.

[21] Romani, G., Ye, Q., Avallone, F., Ragni, D., and Casalino, D., "Numerical Analysis of Fan Noise for the NOVA Boundary-Layer Ingestion Configuration," *Aerospace Science and Technology*, Vol. 96, 2020. https://doi.org/10.1016/j.ast.2019.105532.

[22] "A Method for Estimating Drag-Rise Mach Number at Zero Incidence of Smooth or Bumpy Non-Ducted Axisymmetric Bodies Without or With Fins," Tech. Rep. 74013, IHS ESDU, 1974.

[23] Drew, B., and Jenn, A., "Pressure Drag Calculations on Axisymmetric Bodies of Arbitrary Moldline," *28th Aerospace Sciences Meeting*, 1990. https://doi.org/10.2514/6.1990-280.

[24] Purvis, J. W., and Burkhalter, J. E., "Prediction of Critical Mach number for Store Configurations," *AIAA Journal*, Vol. 17, No. 11, 1979, pp. 1170–1177. https://doi.org/10.2514/3.7617.

[25] Della Corte, B., van Sluis, M., and Gangoli Rao, A., *Results of Overall Configuration Wind Tunnel Testing*, CENTRELINE Public Deliverable D3.02, 2021.

[26] Wieneke, B., "PIV uncertainty quantification from correlation statistics," *Measurement Science and Technology*, Vol. 26, No. 7, 2015, p. 074002. https://doi.org/10.1088/0957-0233/26/7/074002.

[27] Serpieri, J., "Cross-Flow Instability: Flow diagnostics and control of swept wing boundary layers," Ph.D. thesis, Delft University of Technology, 2018.

[28] Della Corte, B., Perpignan, A. A., van Sluis, M., and Rao, A. G., "Experimental and Computational Analysis of Model–Support Interference in Low-Speed Wind-Tunnel Testing of Fuselage-Boundary-Layer Ingestion," *9th EASN Conference*, Vol. 304, 2019. https://doi.org/10.1051/matecconf/201930402020.

[29] Chesnakas, C. J., Taylor, D., and Simpson, R. L., "Detailed Investigation of the Three-Dimensional Separation About a 6:1 Prolate Spheroid," *AIAA Journal*, Vol. 35, No. 6, 1997, pp. 990–999. https://doi.org/10.2514/2.208.

[30] Bissinger, N. C., and Breuer, T., *Basic Principles - Gas Turbine Compatibility - Intake Aerodynamic Aspects*, John Wiley & Sons, 2010. https://doi.org/10.1002/9780470686652.eae487.

[31] Drela, M., "XFOIL: An Analysis and Design System for Low Reynolds Number Airfoils," *Low Reynolds Number Aerodynamics*, edited by T. J. Mueller, Springer-Verlag, 1989, pp. 1–12.

A. Performance of the Bare Fuselage configuration

This section provides a brief analysis of the aerodynamic performance of the bare fuselage (BF) configuration. External balance measurements were taken to investigate the aerodynamic forces and moments acting on the overall configuration at various operating conditions. Fig. 16 shows the coefficients for varying incidence angle (Fig. 16a) and sideslip angle (Fig. 16a). The coefficients presented here take into account the forces and moments acting on the entire aircraft model, the fuselage support strut and the exposed section of the wing struts.

Fig. 16a shows that:

1) C_L increases linearly for $\alpha < 8°$, after which a non-linear behavior is found, probably due to the onset of flow separation on the wings. The tail installation have no meaningful effect on C_L.
2) C_D shows the expected quadratic trend against α, centered around the zero-lift angle. The tail installation increases the C_D with a bias that decreases with α.
3) $C_\mathcal{M}$ linearly increases for $\alpha < 8°$, similarly to C_L. The tail installation has a negligible effect on $C_\mathcal{M}$.

Fig. 16b shows that:

1) C_Y non-linearly increases in modulus with β. Similarly, the VTP contribution linearly increases with β.
2) $C_\mathcal{N}$ linearly increases with β. The contribution of the VTP also linaerly increases with β, due to the side-force produced by the VTP.
3) $C_\mathcal{L}$ non-linearly increases with β. The contribution of the VTP reduces $C_\mathcal{L}$, due to the side-force on the VTP.

To identify the main surface flow features at different operating conditions, the surface flow on the fuselage aft-cone and vertical tail was visualized with a fluorescent oil flow visualization. Fig. 17 shows the surface flow for the BF configuration in cruise conditions ($\alpha = \beta = 0°$). The film oil pattern highlights the formation of a separation line on the fuselage surface in proximity of the tail leading edge, which is linked to the onset of an horseshoe vortex. The vortex structure bends around the tail leading edge and flows alongside the tail root, leading to corner flow separation downstream. Moreover, the oil pattern on the vertical tail shows that the shear-lines curve outboard toward the trailing edge. This is probably due to the onset of crossflow caused by the streamlines curvature typical of swept wings.

Fig. 18 reports the total pressure distribution at the trailing edge of the fuselage of the BF configuration in cruise conditions. The fuselage boundary layer presents a distribution which is largely axisymmetric. The wakes of the VTP and of the fuselage-support strut are clearly visibly on the top and bottom sectors, respectively. At this location, the fuselage boundary layer edge is equal to approximately $r/R_\mathrm{b} = 0.7$.

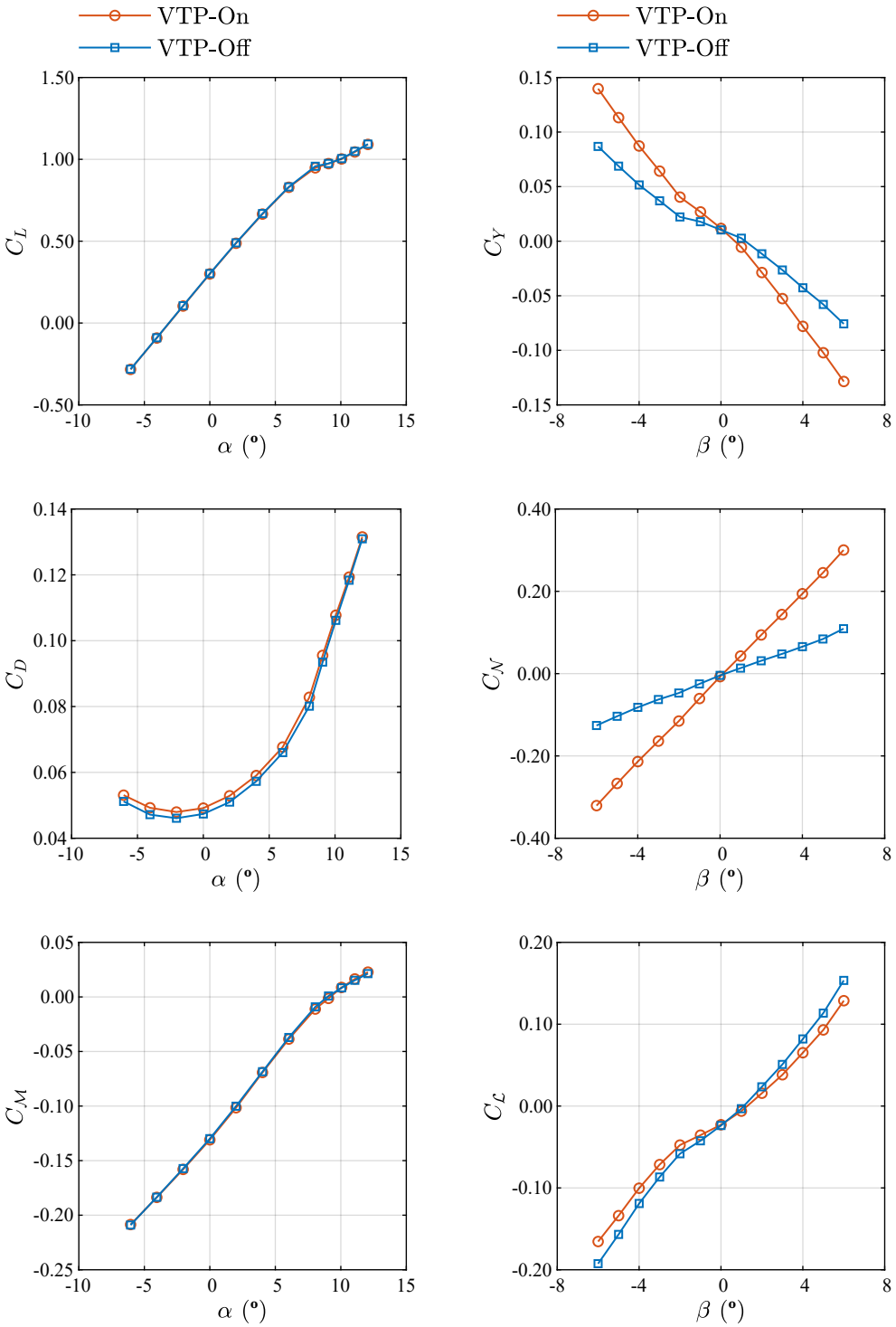

a) Longitudinal equilibrium ($\beta = 0°$) **b) Lateral-directional equilibrium ($\alpha = 0°$)**

Fig. 16 Aerodynamic forces and moments coefficients on the Bare Fuselage configuration. Balance measurements taken at $Re_c = 460,000$.

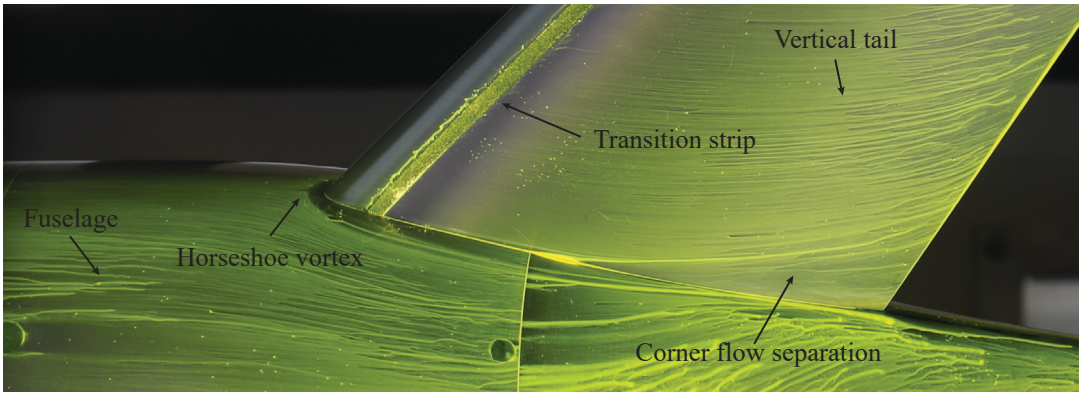

Fig. 17 Surface flow at the fuselage-tail intersection for the Bare Fuselage configuration in cruise conditions. Oil-flow measurements taken at $\alpha = 0° = \beta = 0°$ and $Re_c = 460,000$.

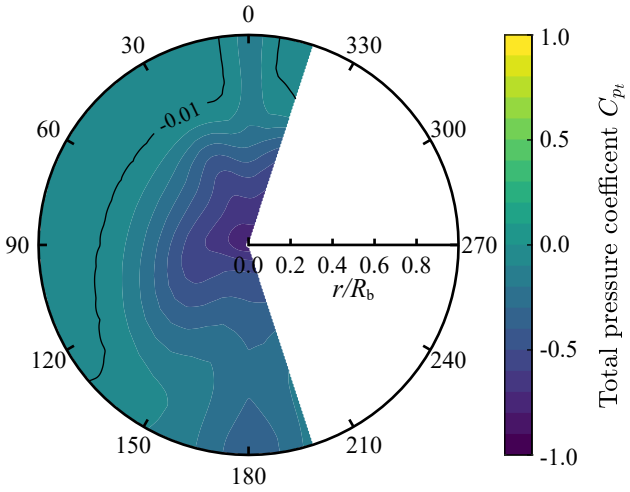

Fig. 18 Total pressure distribution at $x/L = 1$ for the BF, VTP-On case (back view). Total pressure measurements at $\alpha = 0° = \beta = 0°$ and $Re_c = 460,000$.